The Meteoritical Society

*Meteoritics & Planetary Science* 49, Nr 1, 86–94 (2014)
doi: 10.1111/maps.12161

# Inferring asteroid surface properties from radar albedos and circular-polarization ratios

A. VIRKKI[1*], K. MUINONEN[1,2], and A. PENTTILÄ[1]

[1]Department of Physics, University of Helsinki, P.O. Box 64, FI-00014 Helsinki, Finland
[2]Finnish Geodetic Institute, P.O. Box 15, FI-02431 Masala, Finland
[*]Corresponding author. E-mail: anne.virkki@helsinki.fi

*(Received 13 September 2012; revision accepted 10 June 2013)*

**Abstract**–We model electromagnetic scattering from varying closely packed random aggregates of spheres imitating piles of rocks on the surface of an asteroid. We utilize the Multiple Sphere *T*-Matrix Method software to study how different parameters affect the radar albedo and the circular-polarization ratio, for example, the size distribution and electric permittivities of the spherical particles forming the aggregates, and to see if the computed radar albedos and circular-polarization ratios can be linked to the observational data of asteroids detected using radar. The results of the simulations show the radar albedo and the circular-polarization ratio as a function of size parameter for different silicate minerals, including anorthosite, peridotite olivine, and basalt. A direct vacuum-rock surface interface will be considered as well as an approximation for a case in which the rocks are covered by a layer of powdered material, that is, fine regolith. The promising results show values on the range of observed values and imply that the highest circular-polarization values ($\mu_c > 1$) are measurable only for targets with surface material of high electric permittivity ($\varepsilon' > 4.0$). However, the asteroid surface model requires further development before more robust conclusions can be made of the surface chemical and structural composition.

## INTRODUCTION

Radar is a powerful tool for investigating the small bodies of our solar system. The range, measured from the time delay of the echo, and the radial velocity, derived from the Doppler frequency, are the primary measurables of the dynamical properties. With polarimetric measurements, radar can be utilized for determining near-surface physical properties from the circular-polarization ratio. The planetary radar mapping allows studies of not only the top regolith, but also yields information on the structures below the surface. With longer wavelengths, the radar wave is increasingly blind to the smallest particles, as the maximum possible resolution is proportional to the wavelength used. Typical transmitter frequencies are 2380 MHz (S-band) or 8460 MHz (X-band), corresponding to the wavelength of 12.6 or 3.5 cm, respectively.

Using the given frequencies, this study concentrates on rocks with a diameter of about 1–30 cm. (25143) Itokawa is an example of an asteroid imaged with substantially rocky surface (Fig. 1). Whereas the boulders on Itokawa may have diameters of several meters, we consider our size magnitude around 10 cm to be more applicable for wider range of asteroids (compared to, e.g., the surface of (433) Eros).

Electromagnetic scattering provides us with information on the physical properties of the scattering particle or medium. The different scattering characteristics as well as the properties of the incident wave (e.g., the frequency or the polarization) define the information that can be obtained. For example, the circular-polarization ratio, sometimes called the circular depolarization, is a measure of how the asteroid surface depolarizes fully circularly polarized incident radiation. The electromagnetic scattering in small solar system bodies is usually multiple scattering (including some single scattering) from closely packed random media of inhomogeneous particles, that is, regoliths. The physical parameters that define the scattering characteristics in

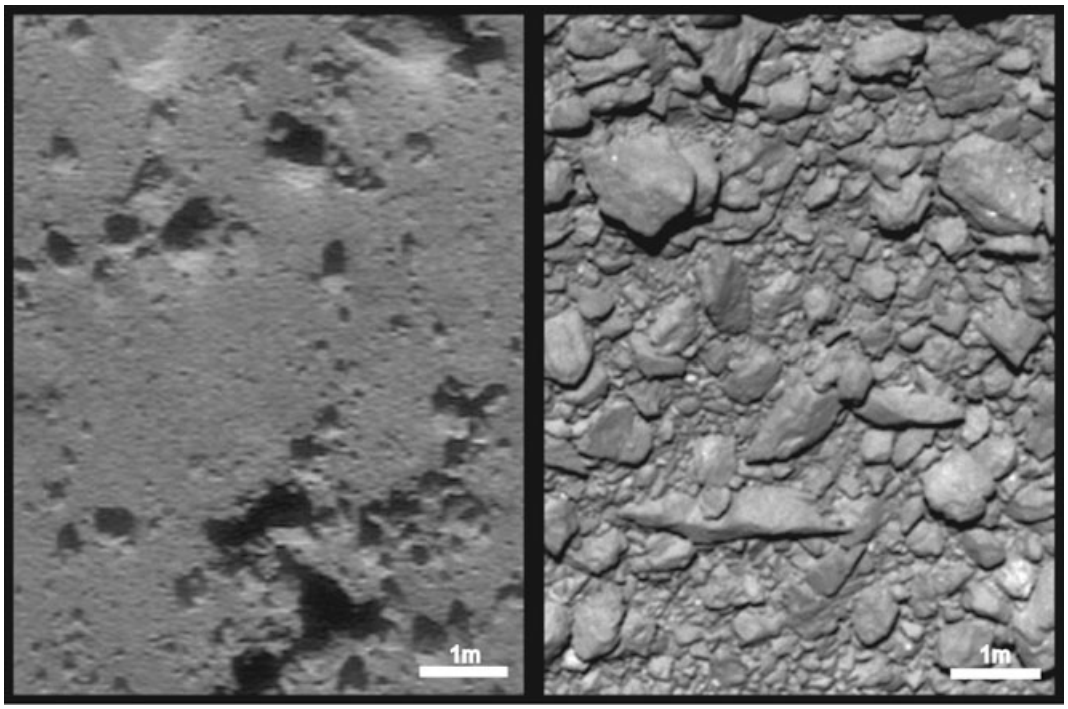


Fig. 1. Example surfaces of asteroids depicting (25143) Itokawa with several large boulders covering the surface (on the top) and (433) Eros with few over meter-size boulders (on the bottom). The resolution is about 2.4 cm per pixel. The scale bar in the lower right corner is 1 m. Picture courtesy: University of Tokyo/JAXA and NASA.

planetary regoliths are, for example, particle size and morphology, surface roughness and porosity of the body, as well as the electric permittivity and the magnetic permeability of the material.

A comprehensive overview on the studies about circular-polarization ratio, multiple scattering, and opposition phenomena was presented in our previous article (Virkki et al. 2012). Virkki et al. (2012), as well as Mishchenko and Hovenier (1995), have shown that the circular and linear polarization ratios depend on the particle size and the refractive index, and cannot be considered only as a measure of particle geometric complexity. In addition, Mishchenko and Hovenier (1995) assess that the linear polarization ratio can be directly related to the circular polarization at backscattering, and, hence, does not require separate treatment. For the interpretation of the results, the comprehensive radar mapping of the Moon is helpful (e.g., Campbell and Campbell 2006; Campbell et al. 2010). The studies show, for example, small areas of circular-polarization ratios near unity associated with small craters.

The major problem with modeling the regolith at microwave frequencies is currently the absence of the frequency-dependent electric permittivity values of many asteroid materials. Consequently, the effect of the mineralogy has been historically a challenge to study. For the minerals known to exist on the Moon there are, however, measurements by Campbell and Ulrichs (1969) that can be utilized here. Because the materials of which the atmosphereless solar system bodies consist have much in common, we can select a few substances that are known to appear also in asteroids, and mix the electric permittivities of these when building the aggregates. As a result, we wish to develop an applicable model and, thus, derive information about the near-surface structure and composition of the small bodies of the solar system.

Nevertheless, there are some points that should be noted considering the values in the paper by Campbell and Ulrichs (1969). First, the measurements have been carried out using 450 MHz and 35 GHz, that is, not for 2.38–8.46 GHz used for the typical asteroid radar observations. However, because for most of the minerals the difference between the two frequencies used is less than the variance of the values measured at 450 MHz, interpolation between the two frequencies should not cause significant error. Second, the metallic content of regolith requires further research in terms of scattering effects. Often, the material is assumed nonmagnetic, but, especially in the case of metallic asteroids, there may be a substantial effect on the scattering of the radar signal.

In the Scattering Theory section, we explain the theory that is required for computing the circular polarization from the output data of the simulations.

Also, the other important measurables will be reviewed. The Observational Data section presents the majority of the current published observation results on circular-polarization ratios and radar albedos of asteroids. The electric permittivities measured for lunar rocks and their significance for asteroids are discussed. The Aggregate Shape Model section describes how the aggregates with polydisperse size distribution were built, and the article concludes with a discussion of the simulation results in comparison to the observations as well as implications for the future research and physical model development.

## SCATTERING THEORY

Small solar system bodies can be observed using radar by measuring the distribution of echo power in time delay and Doppler frequency for a circularly polarized wave, in the same (SC) and opposite circular-polarization state (OC) as compared to the transmitted wave. The total radar albedo ($\hat{\sigma}_{\mathrm{T}}$), or the radar reflectivity, is the total echo power at the backscattering direction. The observation results usually provide us only with the OC radar albedo ($\hat{\sigma}_{\mathrm{OC}}$), which is usually the stronger of the two states, but we also compute, in this study, the total radar albedo: $\hat{\sigma}_{\mathrm{T}} = \hat{\sigma}_{\mathrm{OC}} + \hat{\sigma}_{\mathrm{SC}}$. Thus, a complete image of the reflectivity may be obtained.

The observation reports often also give the radar cross section (proportional to the ratio of the scattered to the incident power density), which is related to the radar albedo so that four times the radar cross section in a specified polarization state divided by the projected area of the target equals the radar albedo of that polarization state. Instead of absolute size of the target, we use the size parameter, that is, the ratio of the size of the particle to the wavelength:

$$x = kr = \frac{2\pi r}{\lambda}, \tag{1}$$

where $r$ is the radius and $k$ the wave number. In this study, the size parameter $x$ refers to the size parameter of the spheres that form the aggregate, that is, the size of one rock on the surface of an asteroid relative to the wavelength of the signal. It is important to pay attention to which size parameter is used in each case. As in the case of nonspherical targets, there are several possibilities to determine the radius. To describe the size parameter of the total aggregate (or the rock pile), we prefer to use the volume size parameter ($x_V$), which refers to a single sphere with volume equal to that of the aggregate. For an aggregate of $N$ spheres with sphere size parameters $x_i$:

$$x_V = \sqrt[3]{\sum_{i=1}^{N} x_i^3}. \tag{2}$$

As a third form of the size parameter, we use $x_{\mathrm{EPA}}$, which is the size parameter of a sphere with a projected area equal to that of the aggregate. This form of size parameter is computed for each aggregate using ray tracing and is only used for determining the radar albedo, whereas $x$ and $x_V$ will be used more later on in the article.

Our simulations of electromagnetic scattering include computing the scattering matrix as explained further in The Aggregate Shape Model section, from which all the scattering parameters can be computed. The $4 \times 4$ scattering matrix describes the scattering properties of a particle or a medium. Here, $P_{\mathrm{nm}}$ refers to normalized and $S_{\mathrm{nm}}$ to unnormalized scattering matrix elements. From the scattering matrix, the total radar albedo can be computed in the following way:

$$\hat{\sigma}_{\mathrm{T}} = \frac{4S_{11}(180^\circ)}{k^2 D_{\mathrm{eff}}^2} = \frac{x_V^2 Q_{\mathrm{sca}} P_{11}(180^\circ)}{x_{\mathrm{EPA}}^2}, \tag{3}$$

where $D_{\mathrm{eff}}$ is the effective diameter of the body and $Q_{\mathrm{sca}}$ is the scattering efficiency, which is the scattering cross section divided by the projected area of the body. The total radar albedo is directly proportional to the microwave band (radar) geometric albedo ($p_{\mathrm{r}}$), that is, $\hat{\sigma}_{\mathrm{T}} = 4p_{\mathrm{r}}$ (Ostro 1993). While the geometric albedo has a Lambertian disk as an object of reference, for radar albedo, a fully conducting sphere is used, having a total radar albedo of unity.

The circular-polarization ratio $\mu_{\mathrm{c}}$ is the ratio of the echo power in the same circular-polarization state to that in the opposite circular-polarization state. If the incident beam is fully circularly polarized, in the case of exact backscattering for ensembles of particles and their mirror particles in random orientation, $\mu_{\mathrm{c}}$ can be presented in terms of the elements of the scattering matrix (see, e.g., Bohren and Huffman 1983) as

$$\mu_{\mathrm{c}} = \frac{\hat{\sigma}_{\mathrm{SC}}}{\hat{\sigma}_{\mathrm{OC}}} = \frac{P_{11}(180^\circ) + P_{44}(180^\circ)}{P_{11}(180^\circ) - P_{44}(180^\circ)}. \tag{4}$$

For any perfectly smooth or symmetric surface, $\mu_{\mathrm{c}} = 0$.

Due to the requirements by the software we use for the simulations, we use the refractive index instead of the electric permittivity. From the relative electric permittivity $\varepsilon_{\mathrm{r}} = \varepsilon' + \mathrm{i}\varepsilon''$ (usually relative to the permittivity of free space, $\varepsilon_0 = 8.854 \times 10^{-12}$ F/m),

Table 1. Data statistics (the number [$N$] of targets, the average, and the standard deviation) of the circular-polarization ratio ($\mu_c$) and the OC radar albedo ($\hat{\sigma}_{OC}$) for the asteroid types of the Tholen classification (Tholen 1989).

| Type | $N$ of $\mu_c$ | Average $\mu_c$ | SD of $\mu_c$ | $N$ of $\hat{\sigma}_{OC}$ | Average $\hat{\sigma}_{OC}$ | SD of $\hat{\sigma}_{OC}$ |
|---|---|---|---|---|---|---|
| S | 90 | 0.250 | 0.151 | 42 | 0.142 | 0.046 |
| C | 36 | 0.151 | 0.110 | 31 | 0.135 | 0.056 |
| B | 5 | 0.242 | 0.167 | 1 | 0.083 | – |
| G | 4 | 0.098 | 0.078 | 4 | 0.082 | 0.041 |
| F | 3 | 0.150 | 0.090 | 2 | 0.150 | 0.004 |
| M | 17 | 0.120 | 0.090 | 14 | 0.294 | 0.135 |
| X | 8 | 0.514 | 0.385 | 4 | 0.220 | 0.194 |
| E | 8 | 0.831 | 0.143 | 4 | 0.253 | 0.110 |
| P | 5 | 0.164 | 0.049 | 2 | 0.063 | 0.003 |
| Q | 12 | 0.274 | 0.107 | 4 | 0.165 | 0.107 |
| V | 6 | 0.550 | 0.141 | 2 | 0.125 | 0.024 |
| D | 1 | 0.160 | – | 1 | 0.110 | – |
| T | 1 | 0.110 | – | 1 | 0.120 | – |

the refractive index $m = n + ik$ can be obtained using the following equations:

$$n = \sqrt{\frac{\sqrt{\varepsilon'^2 + \varepsilon''^2} + \varepsilon'}{2}} \tag{5}$$

$$k = \sqrt{\frac{\sqrt{\varepsilon'^2 + \varepsilon''^2} - \varepsilon'}{2}}. \tag{6}$$

If $\varepsilon'' = 0$, the refractive index is simply $m = \sqrt{\varepsilon'}$. We assume here the relative magnetic permeability $\mu_r = 1$ for all the cases due to the absence of knowledge of more realistic values.

## THE OBSERVATIONAL DATA

Currently, data for over 300 asteroids have been obtained using radar. Table 1 presents the mean and standard deviations of the observed values and Fig. 2 illustrates the data. The data has been gathered mainly from Neese et al. (2012).

The average values of the observed $\mu_c$ measured for different taxonomic types (i.e., the classification based on spectro-photometry) vary depending on the type from 0.10 (G type) to 0.83 (E type). Some spectral types suffer from a small sample size, but none of the types seems to differ distinctly from the others in terms of the lowest $\mu_c$ or $\hat{\sigma}_{OC}$. Instead, a few types seem to have clearly larger values than the rest, that is, E, V, and part of the X type for $\mu_c$, and M, E, and X for $\hat{\sigma}_{OC}$. As high a value as $\mu_c = 1.6$ has been measured for the Jovian moon Europa (Ostro et al. 1980) and later on explained by coherent backscattering (Black et al. 2001). For an asteroid, the maximum value observed using radar is $\mu_c = 1.48 \pm 0.4$ for the asteroid 2003 $TH_2$ Benner et al. (2008). For the known types, the largest values are $\mu_c = 1.10 \pm 0.19$ and $\mu_c = 1.09 \pm 0.06$ for the X-type asteroids (141593) 2002 $HK_{12}$ (Benner et al. 2008) and (17511) 1992 QN (Benner et al. 1997), respectively. Nevertheless, the metallic asteroids have evidently also the widest distribution of values, which may imply that there are near-surface physical properties that affect the radar measurables more than the average, for example, more deviation in the surface structure or the magnetic permeability.

The range of mean $\hat{\sigma}_{OC}$ vary from $\hat{\sigma}_{OC} = 0.06$ (P type) to $\hat{\sigma}_{OC} = 0.27$ (M type). The highest $\hat{\sigma}_{OC} = 0.58$ has been measured for an asteroid (6178) 1986 DA of M type. As has been stated in the Scattering Theory section, a fully conducting sphere is used as an object of reference for radar albedo. Hence, the radar albedo is currently accepted to be a measure of metallicity of an asteroid, so values proportional to the assumed metallicity of the type (high for X and M, low for carbonaceous C and P types) are not a surprise. However, although $\hat{\sigma}_{OC}$ is inversely proportional to $\mu_c$, this is not visible in the observations, and an asteroid with high $\hat{\sigma}_{OC}$ as a result of a high portion of metal inside may have a low or a high $\mu_c$. For example, M type has a high mean, $\hat{\sigma}_{OC}$ but low $\mu_c$, whereas for X type, the mean values of both parameters are moderately high. E type is not considered especially metallic (e.g., Zellner et al. 1977), but it also has moderately high $\hat{\sigma}_{OC}$ and very high $\mu_c$.

Considering which minerals, that is, which electric permittivities, may be found in the asteroids is an important issue for the simulations. For differentiated, nonprimitive achondritic asteroids, basalts are

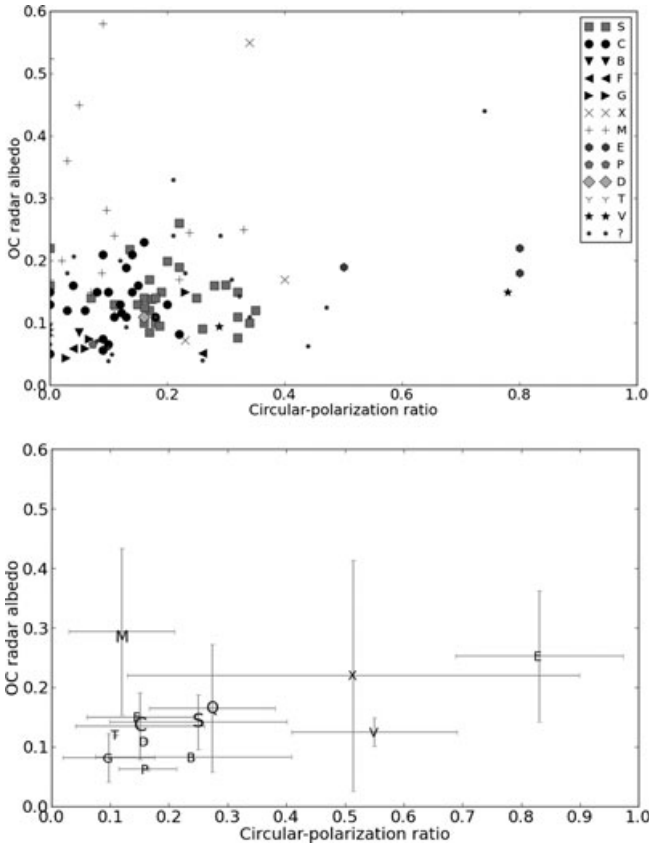


Fig. 2. The circular-polarization ratios versus the OC radar albedos for the different asteroid taxonomic classes. Above, also unknown classes have been included, but only for the asteroids for which both parameters are measured. Below, for the mean values are included all the asteroids for which either one parameter is known. Size of the letter refers to the size of the class in terms of the number of observations. The error bars present the standard deviation.

noteworthy, whereas for silicaceous asteroids, olivine is an important mineral. According to the measurements by Campbell and Ulrichs (1969), the basalts obtain values of $\varepsilon' = 5.3$–$9.6$ (refractive index, $n = 2.30$–$3.10$), for anorthosite and olivine peridotite (dunite) $\varepsilon' = 6.0$–$6.8$ ($n = 2.45$–$2.61$) and for highly porous lava- and ash-based materials such as volcanic ash shale and tuff $\varepsilon' = 2.6$–$2.7$ ($n = 1.61$–$1.64$). The imaginary part $k = 0.01$–$0.03$ for all materials we use. If the material is powdered so that the density is about 1 g cm$^{-3}$, for nearly any material considered here $\varepsilon' \approx 2.0$ ($n \approx 1.4$).

## THE AGGREGATE SHAPE MODEL

For the computations, we use the Multiple Sphere *T*-Matrix Method computer software (MSTM, Mackowski and Mishchenko 2011) that provides an analytical orientation-averaged superposition *T*-matrix solution for the shape model provided. As results, the software gives, for example, the normalized scattering matrix and the scattering efficiencies. Further information on the *T*-matrix method, the aggregates, and the computation times can be found in our previous study (Virkki et al. 2012). The aggregate shape model will, however, be reviewed here shortly for clarity. An example aggregate can be seen in Fig. 3.

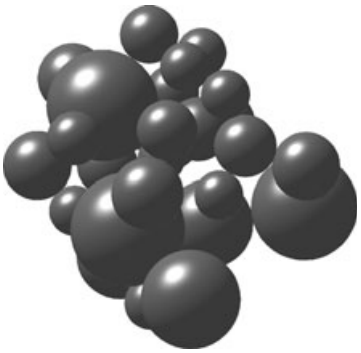

Fig. 3. An example of a polydisperse aggregate.

The polydisperse aggregates (i.e., their size, and, in some cases, the refractive index following some nonuniform distribution) that we use have an effective sphere size parameter $x_e$. This effective size parameter is defined so that the expected volume of the sphere, $E(V[x])$, equals the volume of a sphere of an aggregate with equal-size spheres:

$$E[V(x)] = \int_{x_1}^{x_2} V(y)p(y)\mathrm{d}y = \frac{4}{3}\pi x_e^3, \tag{7}$$

where, for the sphere sizes, we use a truncated power-law distribution

$$p(x) = \frac{k-1}{x_1^{1-k} - x_2^{1-k}} x^{-k}, x \in [x_1, x_2]. \tag{8}$$

Here, $k$ is the power-law index, and $x_1$ and $x_2$ are the lower and upper bounds of the distribution. Hence, the bounds are found by setting the width of the distribution ($w = x_2 - x_1$) to some desired value at $x_e = 2$, and solving for $x_1$ and $x_2$:

$$\int_{x_1}^{x_2} \frac{4}{3}\pi \frac{k-1}{x_1^{1-k} - x_2^{1-k}} y^{3-k}\mathrm{d}y = \frac{4}{3}\pi 2^3. \tag{9}$$

Choosing a power-law index $k = 3$ and distribution widths $w = 1$ or 2 provides us with a distribution $p(x)$ where $x \in [1.58, 2.58]$ or $x \in [1.30, 3.30]$, respectively. The index 3 has been chosen to represent the typical values of 2.5–3.5 for the size distribution of regolith

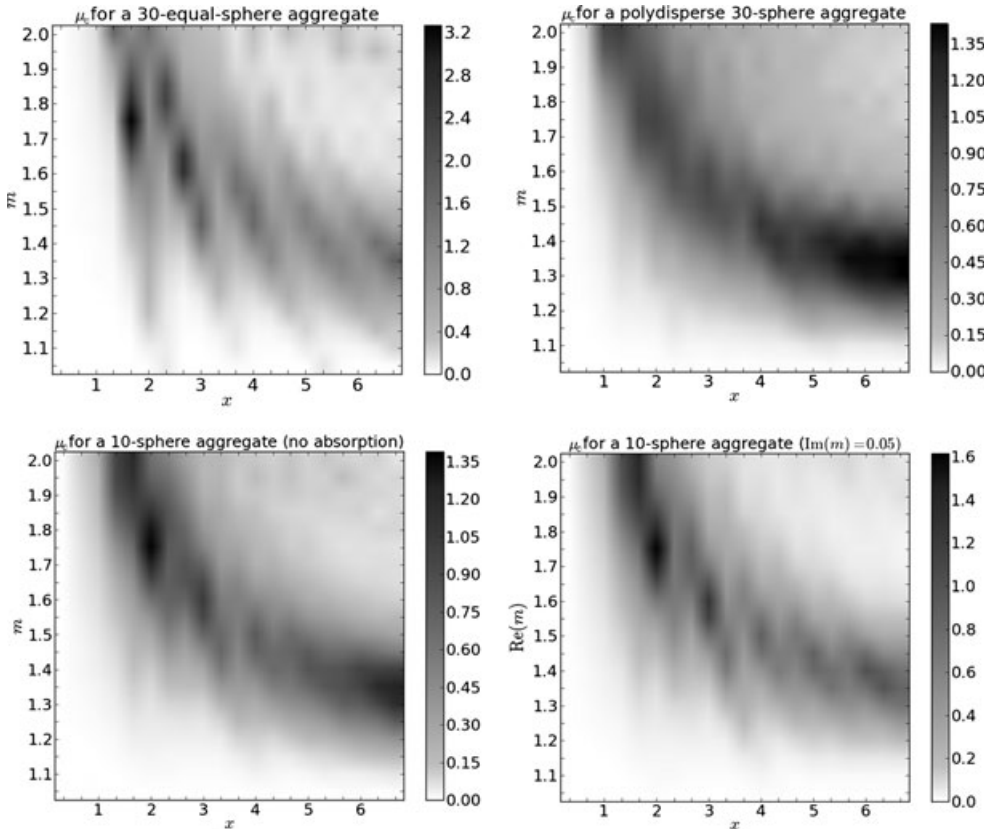


Fig. 4. On the top, the effect of the sphere size parameter and the real part of the refractive index on $\mu_c$ of a 30 equal-sphere aggregate (on the left) and a 30 polydisperse-sphere aggregate (on the right). On the bottom, the effect of the imaginary part of the refractive index ($k$) with values $k = 0$ (on the left) and $k = 0.05$ (on the right) while using the same aggregate geometry for both (10 polydisperse-sphere aggregate). The top row has $k = 0$. All panels consist of 400 data pixels, the data varying in $x = [0.33, 6.67]$ and $m = [1.05, 2.0]$.

particles (see, e.g., Shoemaker and Morris 1968). For other effective size parameters, the sizes of the spheres have been scaled similar to the case with equal-size spheres. Note that, hence, the width of the distribution also changes proportional to the size parameter; for example, doubling or halving the required effective sphere size parameter would, respectively, double or half the width of the size distribution. Therefore, the size distribution widths will be called relative so that a relative size distribution width refers to the width of the distribution at $x_e = 2$. For simplicity, the effective size parameter $x_e$ will be referred to as $x$ hereafter. In this study, the aggregates will be polydisperse and all the computations orientation-averaged by default. The reliability of the computation results due to software was tested by computing a few aggregates using also the discrete-dipole approximation (DDA). The results show some difference: when $m = 1.6$ and $x_V = 6.22$, DDA provides a value of $\mu_c$ 0.1 less than MSTM. For the additional two cases, $m = 1.3$, $x_V = 8.26$, and $m = 2.0$, $x_V = 4.14$ there is a lot less difference: 0.004 and 0.01, respectively. So although some difference occurs, according to our test cases, the error in comparison due to the software is less than 20%.

## RESULTS AND DISCUSSION

Figure 4 reviews some of the computational results of our previous study (Virkki et al. 2012). The panels show clear dependence on the refractive index and the size parameter for the orientation-averaged $\mu_c$ in the backscattering direction. The structure consists of two crossing sets of bands of maxima: the primary band, following approximately the extinction efficiency of a sphere with the same size parameter as the spheres of the aggregate, and the more vertical secondary bands, a result of strong contribution from bisphere resonances between the spheres. Comparing the panels, we see that if the size distribution of the spheres is polydisperse (i.e., the size distribution of the spheres follows the truncated power-law size distribution described before), the secondary bands fade, but the primary band remains, and the maximum value significantly decreases as a result of decreased constructive interference.

In addition, the effect of increased absorption has been presented as an important process, considering applications in the nature. Generally, the absorption ($k = \mathrm{Im}(m)$, proportional to the conductivity of the material) decreases the computed $\mu_c$ proportionally to the size parameter used. Note, however, that the maximum value in the case of $k = 0.05$ is nearly 20% higher than in the case of $k = 0$ with the same aggregate geometry, meaning that, at small size parameters, a small amount of absorption may increase $\mu_c$ to some extent. The comparison between the 30-sphere aggregates in the top row and the 10-sphere aggregates in the bottom row shows that the number of spheres does not affect the structure significantly; spheres of the same size have the same average effect on $\mu_c$ and the number of spheres does not affect the average. Note, however, that the smaller number of spheres fades the secondary bands less than the larger number, which causes some difference between the top and the bottom rows. Also, the range of radii (width of the power-law distribution) of the spheres has a small effect.

In this study, we select certain materials and mix them in terms of the refractive indices of the spheres. The values were chosen as the values of refractive index at 450 MHz. The first value, $m = 2.49 + 0.0124\mathrm{i}$ refers to olivine peridotite (dunite); the second value, $m = 2.6 + 0.0104\mathrm{i}$ to anorthosite; and the third value, $m = 2.7 + 0.0188\mathrm{i}$ to an average value for basalts (here, amygdaloidal basalt). However, the results do not differ significantly from the case of a single mineral only, as there are only small deviations in the values of $m$.

It is also possible to approximate the circular-polarization ratio contributed by rocks immediately under the surface (see Fig. 5). The relative refractive index can be written as $m_r = m/m_e$, where $m_e$ is the refractive index of the material around the rocks, that is, their environment ($m_e = 1.0$ for vacuum). So, inside material with $m_e > 1.0$, the relative refractive index is decreased by a factor of $m_e$. Also, the incident wave should be perpendicular to the surface so that the refraction does not cause any additional effect on polarization, as is the case only for exact forward-scattering. If the layer above is assumed to be smooth (compared to the wavelength), it may increase the opposite-sense part of the echo, but not the same-sense, thus being able to decrease $\mu_c$ to some extent, but not increase. Also, the radar albedo may decrease due to extinction by the layer above. Thus, in this case, the computed values are maximum values and the error depends on the thickness of the layer above.

As an example case, we use olivine peridotite and anorthosite inside, first, semiwelded tuff or volcanic ash shale with $n = 1.6$, and second, powdered material with $n = 1.4$, which is approximately the same for all

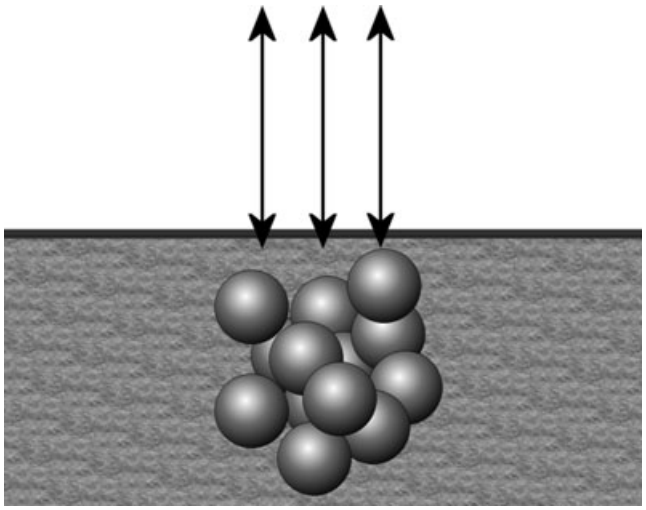

Fig. 5. Visualization of a rock pile under a thin layer of fine regolith. We assume that the refractive index of the aggregate relative to the environment changes the scattering significantly under the surface, but that the interface does not have a significant effect. Above the surface of the asteroid, the environment is considered void.

powdered rocks discussed here, for density of 1 g $\mathrm{cm}^{-3}$ (Campbell and Ulrichs 1969). The imaginary part $k = 0$ for $m_e$ due to restrictions of the simulation software. Thus, $m_r = 1.56 + 0.0124\mathrm{i}$ and $1.63 + 0.0104\mathrm{i}$ for the first case and $m_r = 1.78 + 0.0124\mathrm{i}$ and $1.86 + 0.0104\mathrm{i}$ for the second case. As results, we obtain curves such as in the panels of Fig. 6. Evidently, these also correspond to the case in which the material is on the surface and has the refractive indices given ($m_e = 1$, $m_r = m$). For example, for water ice, $m = 1.78 + 0.002\mathrm{i}$ ($\lambda = 10$ cm and the temperature $-20$ °C, Warren 1984). If $m$ is very close to $m_e$, that is, $m_r \approx 1$, the scattering due to the aggregate becomes neglectable.

The resulting curves (Fig. 6) are predictable by the results of the previous study. The shape does not show any significant deviations from what was obtained for the homogeneous aggregates. The higher refractive indices produce higher circular polarization peaks, and more enhanced decreases after the peaks. For the smaller refractive indices (average $n < 1.8$), the values of $\mu_c$ do not increase above 1.0 in any case. Note that the refractive index of some types of basalts may be up to $n = 3.1$, implying a possibility of even higher peak of maximum $\mu_c$ than is seen for the example case. The second smaller peak that is visible for all cases at about one unit of $x$ larger than for the first peak is likely to be a remnant of the secondary bands discussed previously.

The radar albedos also show very sensible values in comparison to the observed values. Also here, the materials with high refractive index show a sharp increase in $\hat{\sigma}_{OC}$ already for small-sized rocks, but

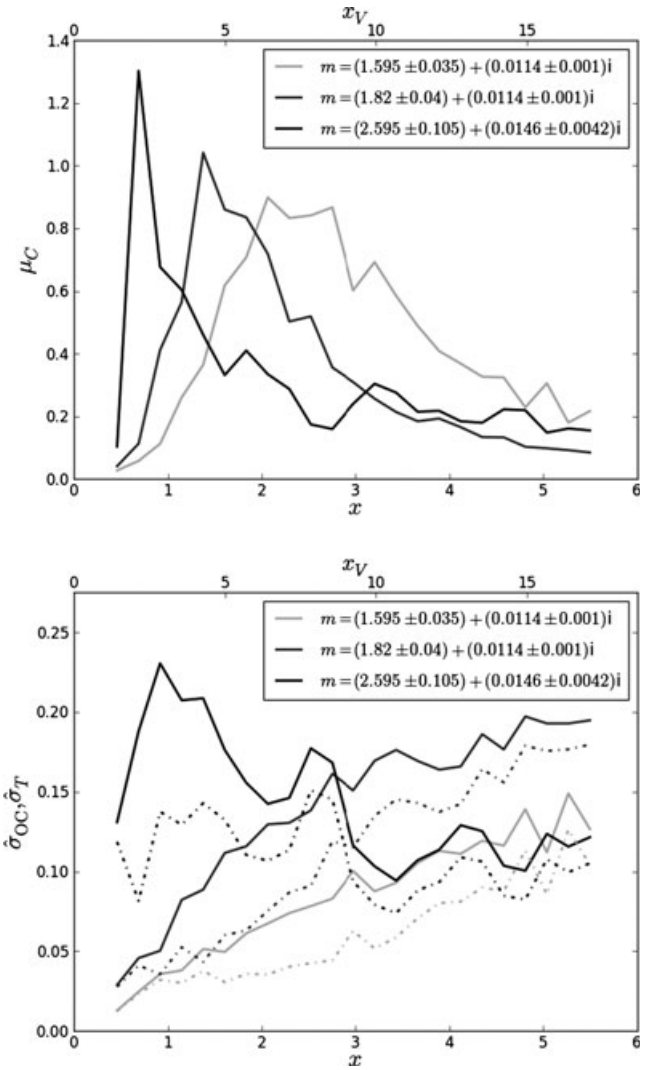


Fig. 6. The circular-polarization ratios (on the top) and radar albedos (on the bottom, dashed line for the OC and solid line for the total) as a function of the effective size parameter for inhomogeneous aggregates ($x$-axis below showing the effective sphere size parameter, and the axis above the corresponding volume size parameter). The curves correspond to $m_r$ = 1.56 + 0.0124i and 1.63 + 0.0104i (light gray), $m_r$ = 1.78 + 0.0124i and 1.86 + 0.0104i (dark gray), and $m$ = 2.49 + 0.0124i, 2.6 + 0.0104i, and 2.7 + 0.0188i (black line). All aggregates have the same geometry as the 30-sphere aggregate in the top right panel of Fig. 4.

remains mainly between 0.08 and 0.15 even for the high size-parameter values, whereas the materials with less refractive index increase proportionally to the size. Note that the absorption affects the observables proportionally to the size parameter, that is, decreasing the values the more the size parameter increases. For the radar albedo, the effect is more evident.

While carrying out these theoretical and numerical simulations, the differences from the actual situations on the asteroid surfaces should be recalled. MSTM uses optically homogeneous and isotropic spheres as scatterers, so some approximations are inevitable. In the case of microwaves, when the wavelength is, for example, 12.6 cm a homogeneous sphere with $x = 5$ would, in reality, be a 20-cm sphere consisting of only one mineral, which is also highly unlikely for natural rocks. Thus, the effect of inhomogeneity will be a topic for further research. The initial tests suggest that the effect is proportional to the deviations from the mean value of the refractive index. For example, 5% deviations in the refractive indices of the aggregate spheres cause about 5% deviations in the parameter values, that is, not significantly more than a different geometry or a small change in the number of spheres would cause.

In addition, the current model does not take into account the interactions with its surroundings. Because $\mu_c$ is multiple-scattering dependent, also the scattering between separate rock piles should be considered. Thus, the challenge for our following study is to simulate interactions between the aggregates used in this study on the surfaces of Gaussian random spheres that imitate the asteroid in the macroscopic scale.

## CONCLUSIONS

In the study, we simulate radar albedos and circular-polarization ratios for asteroid regoliths using aggregates of closely packed spheres. To do this, we utilize simulations of electromagnetic scattering using the MSTM software. The aggregates have a polydisperse size distribution as well as varying compositions. We use the electric permittivities measured for various rock types found on the Moon and select from them the types that are also applicable to asteroids.

The simulated values of $\mu_c$ are in agreement with the values of existing observations. The results suggest that the values of $\mu_c > 1$ require high values of refractive index, that is, $n \geq 2$, and surface structures (rocks) of favorable size. This may explain in part the higher observed values of, for example, vestoids, as the refractive index of basalt is relatively high. Also, the simulated values of $\hat{\sigma}_{OC}$ fit well independent of the rock size. If the surface contains structures of favorable size (compare to the size parameter of our simulations), the circular-polarization ratio may easily increase above 1.0. Then again, if the surface is covered with a layer of powdered or otherwise highly porous material, the circular-polarization ratio remains smaller.

The radar albedos also show very sensible values in comparison to the observed values. Also, here, the materials with high refractive index show a sharp

increase in $\hat{\sigma}_{OC}$ already for small-sized rocks, but remain mainly between 0.08 and 0.15 even for high size-parameter values, whereas the materials with less refractive index increase proportionally to the size. Hence, although radar albedo is a measure of metallicity (i.e., conductivity), also the size of the rocks seems to have an effect. According to our results, the highest OC radar albedos require large structures (relative to the wavelength) for materials with $n < 2$, or, if higher $n$, below the surface inside a material with $n \approx 1.6$ (such as semiwelded tuff). However, this shape model and range of $m$ and $x$ cannot explain values $\hat{\sigma}_{OC} > 0.2$.

As the main conclusion, by the knowledge of radar albedo and circular-polarization ratio, radar can be a helpful tool for taxonomic classification and give implications on the surface structure, especially for the asteroids of unknown types with high values of $\mu_c$. Although the physical model used for the simulations requires further development, the applicable electric permittivities and magnetic permeabilities at microwave frequencies for asteroid material can be constrained by the simulations.

*Acknowledgments*—The research has been supported, in part, by the Academy of Finland (projects 127461 and 257966). We also wish to thank the graduate school of astronomy and space physics for funding of the main author as well as Dr. Evgenij Zubko, Dr. Bruce Campbell, and Dr. John Harmon for their helpful comments.

*Editorial Handling*—Dr. Carle Pieters

## REFERENCES

Benner L. A. M., Ostro S. J., Giorgini J. D., Jurgens R. F., Mitchell D. L., Rose R., Rosema K. D., Slade M. A., Winkler R., Yeomans D. K., Campbell D. B., Chandler J. F., and Shapiro I. I. 1997. Radar detection of near-Earth asteroids 2062 Aten, 2101 Adonis, 3103 Eger, 4544 Xanthus, and 1992 QN. *Icarus* 130:296–312.

Benner L. A. M., Ostro S. J., Magri C., Nolan M. C., Howell E. S., Giorgini J. D., Jurgens R. F., Margot J. L., Taylor P. A., Busch M. W., and Shepard M. K. 2008. Near-Earth asteroid surface roughness depends on compositional class. *Icarus* 198:294–304.

Black G. J., Campbell D. B., and Nicholson P. D. 2001. Icy Galilean satellites: Modeling radar reflectivities as a coherent backscatter effect. *Icarus* 151:167–180.

Bohren C. F. and Huffman D. R. 1983. *Absorption and scattering of light by small particles*. New York: John Wiley & Sons, Inc.

Campbell B. A. and Campbell D. B. 2006. Regolith properties in the south polar region of the Moon from 70-cm radar polarimetry. *Icarus* 180:1–7.

Campbell M. J. and Ulrichs J. 1969. Electrical properties of rocks and their significance for lunar radar observations. *Journal of Geophysical Research* 74:5867–5881.

Campbell B. A., Carter L. M., Campbell D. B., Nolan M., Chandler J., Ghent R. R., Ray Hawke B., Anderson R. F., and Wells K. 2010. Earth-based 12.6 cm wavelength radar mapping of the Moon: New views of impact melt distribution and mare physical properties. *Icarus* 208:565–573.

Mackowski D. W. and Mishchenko M. I. 2011. A multiple sphere T-matrix Fortran code for use on parallel computer clusters. *Journal of Quantitative Spectroscopy & Radiative Transfer* 112:2182–2192.

Mishchenko M. I. and Hovenier J. W. 1995. Depolarization of light backscattered by randomly oriented nonspherical particles. *Optics Letters* 20:1356–1358.

Neese C., Benner L. A. M., and Ostro S. J., eds. Asteroid Radar V18.0. EAR-A-5-DDR-RADAR-V18.0. NASA Planetary Data System, 2012.

Ostro S. J. 1993. Planetary radar astronomy. *Reviews of Modern Physics* 65:1235–1295.

Ostro S. J., Campbell D. B., Pettengill G. H., and Shapiro I. I. 1980. Radar observations of the icy Galilean satellites. *Icarus* 44:431–440.

Shoemaker E. M. and Morris E. C. 1968. Size-frequency distribution of fragmental debris. Surveyor Project Final Report, NASA Technical Report. pp. 32–1265.

Tholen D. J. 1989. Asteroid taxonomic classifications. In *Asteroids II*, edited by Binzel R. P., Gehrels T., and Matthews M. S. Tucson, Arizona: Academic Press. pp. 1139–1150.

Virkki A., Muinonen K., and Penttilä A. 2012. Circular polarization of spherical-particle aggregates at backscattering. *Journal of Quantitative Spectroscopy & Radiative Transfer* 126:150–159, doi:10.1016/j.jqsrt.2012.08.029.

Warren S. G. 1984. Optical constants of ice from the ultraviolet to the microwave. *Applied Optics* 23:1206–1225.

Zellner B., Leake M., Williams J. G., and Morrison D. 1977. The E asteroids and the origin of the enstatite achondrites. *Geochimica et Cosmochimica Acta* 41:1759–1767.